Microwave CAD Circuit Modeling of a Traveling-Wave Electroabsorption Modulator

Robert Lewén, Stefan Irmscher, and Urban Eriksson

***Abstract*—Conformal-mapping techniques are used to derive an effective and advanced calculation model for the microwave properties of a light-intensity traveling-wave electroabsorption modulator, resulting in a quasi-TEM computer-aided-design circuit model. For a given device geometry, the model provides the transmission-line (TML) parameters' characteristic impedance and waveguide (WG) propagation constant. Closed-form expressions are derived for the reactive circuit elements. The calculation model includes both the effect of metal conduction loss, as well as losses due to induced currents in the semiconductor substrate. We treat both the buried heterostructure, as well as the ridge-mesa optical WG implementations. The model is validated with full-wave simulations and compared to measured TML parameters.**

***Index Terms*—Coplanar waveguides (CPWs), electroabsorption, intensity modulation, optical modulation, skin effect, substrate losses, traveling wave.**

I. Introduction

TRAVELING-WAVE electroabsorption modulators (TWEAMs) are attractive solutions due to their potential for high speed combined with high efficiency, and their process compatibility with semiconductor (SC) lasers. This makes them suitable components in high-speed fiber-optic links. High-speed TWEAMs with lengths of over 200 μm exhibit small-signal modulation bandwidths exceeding 40 GHz [1]–[4].

The traveling-wave (TW) configuration offers the possibility to overcome the *RC* time-constant bandwidth limitation of a traditional lumped electroabsorption modulator (EAM) [4]. However, the design of TWEAMs remains challenging. The conflicting requirements for a high ON/OFF ratio, 50-Ω modulator impedance (if possible), and high modulation bandwidth have to be met. This can only be achieved by carefully optimizing the geometry of the devices, which requires a reliable quantitative simulation tool.

A drawback of the TW configuration is that the characteristic impedance of the *microwave* waveguide (WG) is typically significantly less than 50 Ω [2]–[5]. For example, an *optical* WG formed by an active intrinsic layer with a thickness of 0.3 μm and a mesa width of 1.5 μm normally results in a WG impedance between 15–25 Ω. Higher impedance can only be achieved by increasing the intrinsic layer thickness and/or by narrowing the mesa, which consequently requires a higher driving voltage since the modulating electrical field and/or the optical confinement factor have been reduced.

Furthermore, correct termination impedance (matched load) is crucial for operation in the TW regime [3]–[6]. Using high termination impedance results in a reflection that significantly reduces the device bandwidth [5]. With higher impedance mismatch, the bandwidth ultimately becomes limited by the WG capacitance and the performance is similar to a lumped device (with the same capacitance per unit length). Thus, the TW configuration offers an advantage over a lumped configuration only when the load impedance is reduced to match the WG impedance. For an ideally matched TW device, attenuation and velocity mismatch limit the bandwidth of the device, where the attenuation is normally the dominating limitation for the EAM.

For a general transmission line (TML),$n_e = c_0 Z_0 C$ [7][1] where n_e is the microwave index, c_0 is the velocity of light, Z_0 is the characteristic WG impedance, and C is the associated capacitance per unit length. Hence, once the capacitance is given from the optical WG, there exists a tradeoff between designing for a high-impedance (high inductance) or low-velocity mismatch (low inductance) [6]. Furthermore, a high microwave index is often associated with a high propagation loss (high attenuation). Therefore, for a fixed capacitance, a high-bandwidth design does inevitably result in a low modulator WG impedance.

The above discussion indicates the importance of a design tool that can accurately model the electrical WG parameters of an EAM structure, i.e., the characteristic impedance and propagation constant. Analytical formulas readily available for microstrip lines and coplanar waveguides (CPWs) on dielectric substrates [7] fail to describe the properties of an EAM-WG because of the presence of thick semiconductive layers. The loss factors generated by these layers have to be modeled in a quantitative precise manner in order to accurately predict the performance of a device. Full-wave analysis [8]–[10] is the correct approach for solving this problem. However, full-wave analysis is computationally expensive, and commercially available tools are often impractical for simulating a specific structure over a wide range of geometry parameters. Furthermore, numerical problems can occur, such as singularities in the current distribution at sharp corners of conducting structures [11].

Manuscript received April 23, 2002; revised November 15, 2002.

R. Lewén is with the Laboratory of Photonics and Microwave Engineering, Royal Institute of Technology, 164 40 Kista, Sweden and also with Optillion AB, SE-117 94 Stockholm, Sweden.

S. Irmscher is with the Laboratory of Photonics and Microwave Engineering, Royal Institute of Technology, 164 40 Kista, Sweden.

U. Eriksson was with the Laboratory of Photonics and Microwave Engineering, Royal Institute of Technology, 164 40 Kista, Sweden. He is now with Optillion AB, SE-117 94 Stockholm, Sweden.

Digital Object Identifier 10.1109/TMTT.2003.809669

[1]Especially Appendix III and Chapter 3.12.

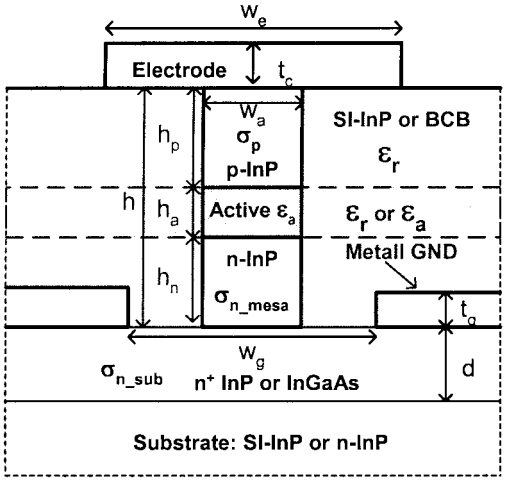

Fig. 1. Typical TWEAM structure [4], [6], [8]. This figure illustrates a BH configuration. The ridge-mesa configuration is represented with $h_n = 0$. The permittivity of the cladding is assumed to be ε_r for a buried WG, and ε_a for a ridge WG.

The electrical WG of a typical TWEAM structure can be well described by a quasi-TEM equivalent-circuit model [5]. With a model like this, characteristic impedance, propagation constant, and also the optical small-signal modulation response can easily be obtained [4]–[6] provided that the circuit element values are known. For a fast modeling tool, it is desirable to find closed formulas allowing the computation of these circuit element values directly from the geometry of the structure.

In this paper, we present a complete set of formulas describing a quasi-TEM circuit model suitable to simulate the microwave properties of a typical TWEAM structures. Previous work includes simplified models based on a parallel-plate approximation [10] combined with a CPW approximation [12]. We use a conformal-mapping approach to derive expressions for a general TWEAM structure (Fig. 1) without simplifying the cross-sectional geometry. Approximations are made when justified and leading to simpler mathematical expressions. The model is compared to full-wave solutions obtained with commercial software (HFSS).

II. Circuit Model

A typical cross section of an EAM TML is illustrated in Fig. 1. The corresponding geometry values and typical material data are listed in Tables I and II, respectively. Our model includes the buried heterostructure (BH) configuration, as illustrated in this figure, as well as a ridge-mesa structure with $h_n = 0$. We find this geometry representative for a number of demonstrated devices, e.g., [1]–[4], [13]. For our case study, we use data for the InP/InGaAsP material system according to published devices [4], [6], [8]. However, the model as such is not restricted to this material system.

The propagation parameters for the TWEAM are described by a slight modification of the model presented in [5]. The network in Fig. 2 describes a unit length of a TML section, with circuit parameters serial impedance per unit length (Z_S) and parallel admittance per unit length (Y_P). From Fig. 2, we obtain

$$Z_S(\omega) \approx j\omega L + (R_C + R_{CG}) + \omega^2 \frac{L^2}{R_{\rm SC}} \qquad (1)$$

TABLE I
Geometrical Dimensions Included in the Calculation Model, With Corresponding Typical Values Used for Calculation Examples. The Two Different Values for h and h_n Represents the Ridge-Mesa and BH Configuration, Respectively

mesa height	h	2.3 or 4.3μm
n-mesa height	h_n	0 or 2μm
p-mesa height	h_p	2μm
active layer height	h_a	0.3μm
mesa width	w_a	2μm
electrode width	w_e	6μm
ground plane slot width	w_g	8μm
conductor thickness	t_c	1μm
ground metal thickness	t_g	0.3μm
semiconductor ground thickness	d	1μm

TABLE II
Assumed Material Data Used for Calculations [14]

Material	Relative Permitivity (ε_r)	Conductivity (σ) [Ω^{-1}cm^{-1}]
n-InP (10^{18} cm^{-3})	12.4	370
p-InP (10^{18} cm^{-3})	12.4	15
semi insulating (SI)-InP	12.4	-
active (InGaAsP)	13.8	-
BCB	2.7	-
gold	1	$4.54*10^5$

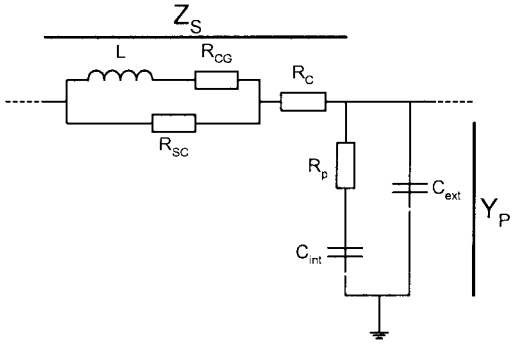

Fig. 2. Equivalent circuit for a unit length of the TML.

where we have assumed that $R_{\rm SC} \gg \omega L > R_{CG}$. R_C and R_{CG} are the conductor loss for the strip and the ground-plane metal, respectively. Both conductor-loss elements are proportional to $\omega^{1/2}$. We also include an additional resistance $R_{\rm SC}$, which represents the loss arising from a longitudinal induced current in the SC material [9]. Note that the term representing the SC loss is proportional to ω^2 and typically dominates at high frequencies, whereas the metal losses dominate at low frequencies [15]. In Section IV-E, we present a more advanced model extending the validity to higher frequencies, as well as for lower values of $R_{\rm SC}$. The latter case is relevant when a conductive substrate is used. From Fig. 2, we find

$$Y_p(\omega) = \frac{j\omega C_{\rm int}}{1 + j\omega C_{\rm int} R_p} + j\omega C_{\rm ext}. \qquad (2)$$

The corresponding characteristic impedance and propagation constant are expressed as

$$Z_0(\omega) = \sqrt{\frac{Z_s(\omega)}{Y_p(\omega)}} \tag{3}$$

$$\gamma(\omega) = \alpha(\omega) + j\beta(\omega) = \sqrt{Z_s(\omega) Y_p(\omega)}. \tag{4}$$

According to our experience, this circuit model provides a good fit for measured electrical TWEAM parameters (Section V-B). This model has also been successfully applied to predict the optical small-signal response at moderate levels of optical input power, using model parameters obtained from electrical microwave measurements [4], [6], [8]. For high levels of optical input power, the induced photocurrent can be modeled by adding an additional resistance or current source in parallel with the internal capacitance [5].

In the remainder of this paper, we show how the value of each circuit element in Fig. 2 can be calculated from the geometry in Fig. 1 by using conformal-mapping techniques.

III. Parallel Admittance Network (Y_P)

A. Capacitances for a Buried WG

Assuming perfectly conducting SC layers, we first calculate the total capacitance of the structure in Fig. 1. Subsequently, this capacitance can be divided into two parts (Fig. 2), one external associated with the metal strip and part of the mesa walls, and one internal associated to the depletion layer and the region around it.

The total capacitance per unit length is obtained as the superposition of the capacitances of the depletion layer ($C_a = \varepsilon_0 \varepsilon_a w_e / h_a$) and of an ordinary microstrip line (C_{strip}) [7], plus a correction (C_{corr}). C_{corr} accounts for the capacitance formed between the perfectly conductive mesa walls plus the fringing field around the depletion layer as follows:

$$C_{\text{total}} = C_{\text{ext}} + C_{\text{int}} = C_{\text{strip}}(w_e, h, t_c, \varepsilon_r) + C_{\text{corr}} + C_a. \tag{5}$$

In order to approximate C_{corr}, we use the following Schwarz–Christoffel transformations (Fig. 3):

$$\frac{dZ}{dW} = \frac{h}{\pi} \frac{1}{\sqrt{1 - W^2}} \tag{6}$$

$$\frac{dZ'}{dW} = \frac{1}{\sqrt{u_1^2 - W^2}}. \tag{7}$$

The field disturbance from the mesa walls is approximated by transforming a parallel-plate capacitance in the right-hand-side figure to the geometry in the left-hand-side figure in Fig. 3. From this capacitance, we obtain C_{corr} by subtraction of $\varepsilon_0 \varepsilon_r w_e / h$ (the capacitance of the electrode strip without fringing field, mesa, and depletion layer) since this part is already included in C_{strip}

$$C_{\text{corr}} \approx \varepsilon_r \varepsilon_0 \left(\frac{2}{\pi} \cosh^{-1}\left(\frac{u_2}{u_1}\right) - \frac{w_e}{h} \right) \tag{8}$$

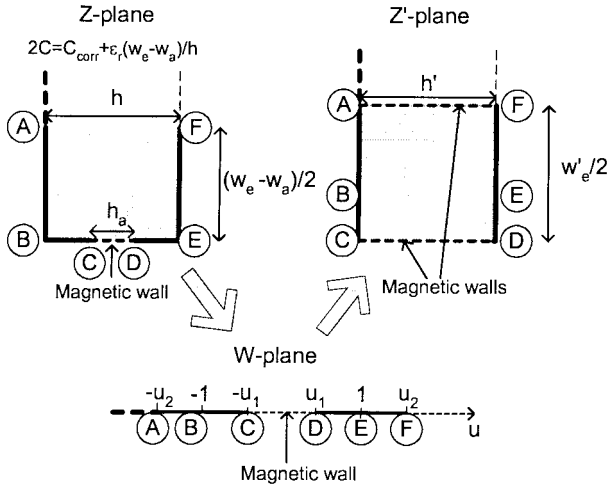

Fig. 3. Schwarz–Christoffel transformation between the W- and Z-plane and the Z'-plane, respectively.

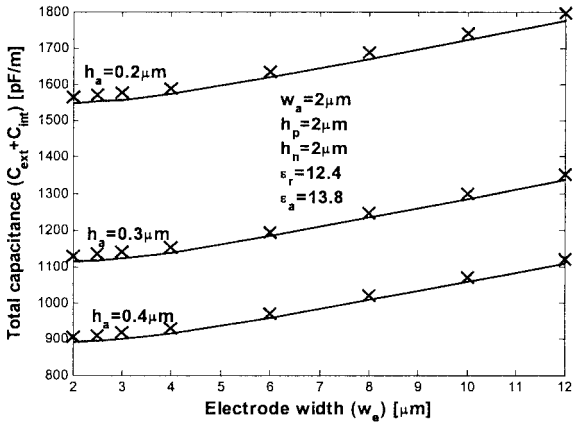

Fig. 4. Simulated (crosses) and calculated (solid lines) total capacitance for a BH modulator configuration with semi-insulating regrowth.

where

$$u_1 = \sin\left(\frac{\pi h_a}{2h}\right) \tag{9}$$

$$u_2 = \cosh\left(\frac{\pi (w_e - w_a)}{2h}\right). \tag{10}$$

Fig. 4 compares the model approximation with the resulting capacitance from HFSS. This capacitance is obtained from the simulated Z_0 and γ by replacing all conductive material to perfect conductors and using (3) and (4).

The split of the total capacitance into C_{int} and C_{ext} (Fig. 2) is important since the series resistance R_p has a major contribution to the WG attenuation, and the $R_p C_{\text{int}}$ product can limit the device bandwidth severely . C_{act} contributes only to C_{int}. With the capacitance of the mesa walls, C_m (Fig. 5, i.e., BC to DE in Fig. 3) it becomes more complicated since an accurate description would require a distributed $R_p - C_m$-model

$$C_m = \frac{2\varepsilon_r \varepsilon_0}{\pi} \cosh^{-1}\left(\frac{1}{u_1}\right). \tag{11}$$

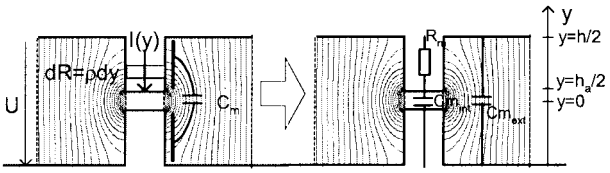

Fig. 5. Splitting C_m into internal and external parts.

Here, we will divide the capacitance so that the lumped model gives the same potential drop due to the mesa resistance. Assuming $\omega C_{\rm int} R_p \ll 1$, we may divide the internal and external capacitance so that

$$\int I(y)\,dR = \frac{j\omega Cm_{\rm int} R_p U}{1+j\omega Cm_{\rm int} R_p} \approx j\omega Cm_{\rm int} R_p U. \quad (12)$$

With $R_p = \rho(h-ha)$, $I_{\rm tot} \approx j\omega C_m U$ and

$$\frac{I(y)}{I_{\rm tot}} = \frac{C(y)}{C_m} = \frac{\cosh^{-1}\left(\frac{1}{u_1}\sin\left(\frac{\pi y}{h}\right)\right)}{\cosh^{-1}\left(\frac{1}{u_1}\right)}. \quad (13)$$

This results in

$$\frac{Cm_{\rm int}}{Cm} = \frac{2}{(h-h_a)\cosh^{-1}\left(\frac{1}{u_1}\right)}\int_{h_a/2}^{h/2}\cosh^{-1}\left(\frac{1}{u_1}\sin\left(\frac{\pi y}{h}\right)\right)dy. \quad (14)$$

The integral has to be evaluated numerically. However, it is easily verified from (9) and (14) that, for a ratio of h_a/h between 0.05–0.5, the ratio of $Cm_{\rm int}/Cm$ varies between 0.83–0.79, thus,

$$C_{\rm int} \approx C_{\rm act} + 0.8C_m \quad (15)$$

$$C_{\rm ext} \approx C_{\rm strip} + C_{\rm corr} - 0.8C_m. \quad (16)$$

B. Capacitances for a Ridge-Mesa Structure With an Extended Active Layer

In this section, we treat the capacitance for an optical ridge-WG structure where the mesa etch stops at the boundary of the active layer (extended active layer). In order to make the geometry similar to the buried WG structure treated in the former section, we have added an image structure mirrored in the ground plane.

The interface between the two dielectric regions, i.e., the cladding layer (BCB, $\varepsilon_r \approx 2.7$) and the active layer (InGaAsP, $\varepsilon_a \approx 13.8$), causes a complication for analytical treatment. We may, however, simplify the problem by treating the boundary as either a magnetic wall (parallel capacitive addition) or an electric wall (serial capacitive addition) [16]. The field lines that originate in the region around the metal strip are essentially perpendicular to the dielectric interface, which is why we approximate this as an electric wall. Hence, adjusting the height of the active layer as $h'_a = 2h_a\varepsilon_r/\varepsilon_a$ and $h' = 2h_p + h'_a$ approximates the contribution to the *external* capacitor (Fig. 6). The corresponding capacitance given from (8)–(10) is then half the value of the actual capacitance, e.g., $C_{\rm corr} = 2 \cdot C'_{\rm corr}$, where $C'_{\rm corr}$ is obtained from (8).

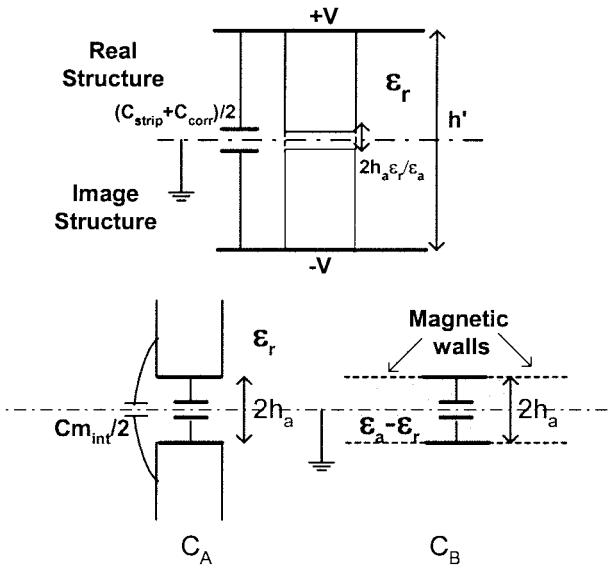

Fig. 6. Configuration for capacitance calculation for a ridge-mesa structure with an extended active layer. The upper geometry shows the configuration for the approximation of the external capacitance, where the active layer thickness has been modified according to the ratio between the dielectric constant for each material. The lower figures illustrate the configuration for the internal capacitance.

The field lines that originate in the vicinity of the active region are essentially parallel to the dielectric interface, which is why we treat this as a parallel capacitive addition. First, we calculate the *internal* capacitance replacing all dielectric with ε_r and then repeat the analysis according to the former section

$$C_A \approx \varepsilon_r\varepsilon_0\left[0.8^*\frac{4}{\pi}\cosh^{-1}\left[\frac{1}{\sin\left(\frac{\pi h_a}{2h}\right)}\right] + \frac{w_a}{h_a}\right]. \quad (17)$$

Second, we include the additional capacitance due to the higher dielectric constant in the active layer by replacing the interface with a magnetic wall and adjusting the dielectric constant [17]

$$C_B \approx 2(\varepsilon_a - \varepsilon_r)\varepsilon_0\frac{K'(k_r)}{K(k_r)} \quad (18)$$

$$k_r = \frac{1}{\cosh\left(\frac{\pi w_a}{4h_a}\right)}. \quad (19)$$

where K is the complete elliptic integral of the first kind [7]. In the remainder of this paper, we will use the notation $K = K(k)$ and $K' = K'(k) = K(k') = K\left(\sqrt{1-k^2}\right)$.

The total internal capacitance is finally given as the sum of both contributions $C_{\rm int} = C_A + C_B$. The correspondence to the capacitance obtained from HFSS is shown in Fig. 7.

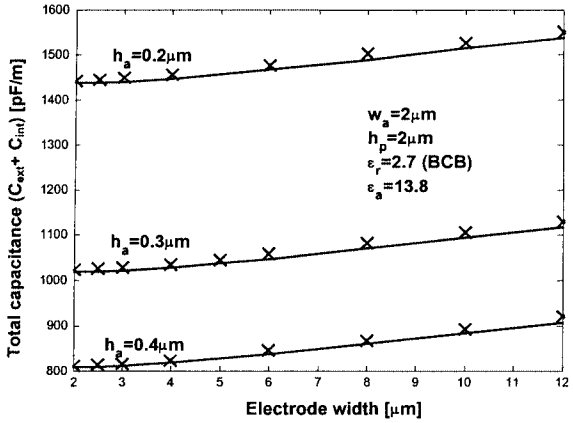

Fig. 7. Simulated (crosses) and calculated (solid lines) total capacitance for a ridge-mesa structure with an extended active layer (ridge WG).

C. Admittance Loss

In the InP/InGaAsP material system, the major contribution to the TML attenuation arises from the serial resistance (R_p) in the admittance network in Fig. 2, which we approximate as

$$R_p = \frac{h_p}{w_a \sigma_{p\text{-InP}}} + \frac{h_n}{w_a \sigma_{n\text{-mesa}}} + \frac{w_g}{4d\sigma_{n\text{-sub}}}. \tag{20}$$

where h_p and h_n is the thickness of the p- and n-layer within the mesa, respectively (Fig. 1). In the normal case, R_p is dominated by the p section, i.e., the first term in (20).

The influence of R_p is not only important for the TML attenuation, but it also indicates that the voltage over the active layer is not the same as the voltage at the electrode [5]. This can have a strong impact on the optical modulation at higher frequencies.

Also note that the conductivity of the n-*doped* material affects both R_P and R_{SC} (Fig. 2). For a low contribution to R_P, the conductivity should be high. However, a high conductivity leads to an increased loss due to induced SC current modeled by R_{SC}, as we will see in Section IV. Hence, there is an optimum value for the n-doping, leading to minimized microwave attenuation.

IV. Serial Impedance Network (Z_S)

A. Inductance Model

It is well known [10], [15], [18], [19] that a TML consisting partly of SC material, in a low-frequency regime, supports so-called slow-wave modes as the skin depth of the SC typically exceeds the dimensions of the device. For the basic quasi-TEM model, the value for the inductance is approximated by replacing all doped SC material with dielectric and use the relation [7], [15]

$$LC_{\text{air}} = \mu_0 \varepsilon_0 = \frac{1}{c_0^2} \tag{21}$$

where C_{air} is the capacitance per unit length when all dielectric and SC material is replaced by air (*in vacuo capacitance*).

Depending on the ground slot width (w_g in Fig. 1), the geometry of the EAM TML resembles something in between the two extremes of a microstrip (small w_g) and a CPW (large w_g). The value of C_{air} can be calculated exactly for an arbitrary configuration between these two extremes by the use of conformal-mapping techniques, which is essentially the same problem as treated in [11]. For a more comprehensive study of different electrode implementations, we recommend this paper as a complement to our model. In this paper, we will simplify the analysis by introducing an additional mirrored *virtual conductor* positioned at $x = -h$ (see Fig. 8). This modification will enable us to do a number of approximations facilitating the calculation of the inductance and corresponding conductor-loss elements in Fig. 2 (see Section IV-C).

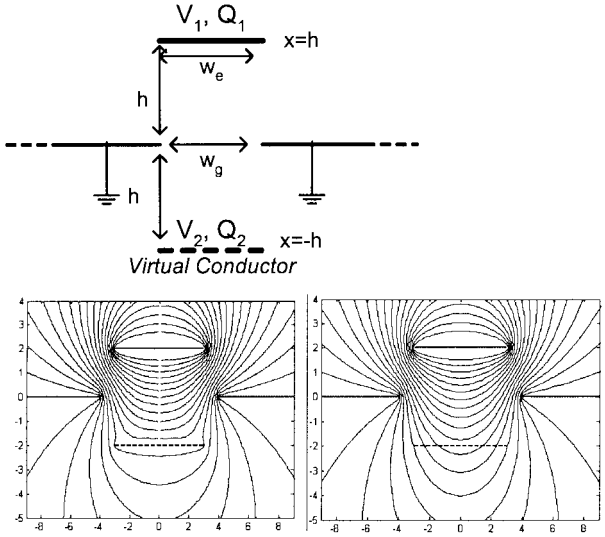

Fig. 8. Upper figure illustrates the configuration of the virtual conductor. The lower figure illustrates calculated magnetic field with (*left-hand side*) and without (*right-hand side*) the presence of the virtual conductor, respectively.

The charge accumulated on each conductor is given as

$$\begin{pmatrix} Q_1 \\ Q_2 \end{pmatrix} = \begin{pmatrix} c_{11} & c_{12} \\ c_{21} & c_{22} \end{pmatrix} \begin{pmatrix} V_1 \\ V_2 \end{pmatrix}. \tag{22}$$

The electromagnetic (EM) field may be expressed as the superposition of the following two orthogonal modes.

- *Even mode*: $Q_1 = Q_2 = Q_{\text{even}}$ and $V_1 = V_2 = V_{\text{even}}$.
- *Odd mode*: $Q_1 = -Q_2 = Q_{\text{odd}}$ and $V_1 = -V_2 = V_{\text{odd}}$.

We define the corresponding capacitances as $C_{\text{even}} = Q_{\text{even}}/V_{\text{even}}$ and $C_{\text{odd}} = Q_{\text{odd}}/V_{\text{odd}}$.

We obtain C_{air} for the case when there is no net charge on the lower conductor $(Q_2 = 0)$, which results in the relation

$$C_{\text{air}} \approx \frac{Q_1}{V_1} = \frac{2C_{\text{even}}C_{\text{odd}}}{C_{\text{even}} + C_{\text{odd}}}. \tag{23}$$

This is equivalent to the case when there is no current transport in the lower conductor, i.e., $I_2 = 0$, thus, $I_{\text{even}} = I_{\text{odd}} = I_{\text{tot}}/2$ (hence, the term *virtual* conductor). Even if we do not allow any current transport or charge accumulation on the lower conductor, it will still act as an equipotential line in the cross section of the structure (Fig. 8). The charge distribution within this cross section is allowed to change why the field will be distorted compared to the original configuration (without the virtual conductor). However, this distortion is essentially a local phenomenon in a region close to the virtual conductor. The presence of the virtual conductor has typically a very small effect on the general field solution, especially in the upper half-plane

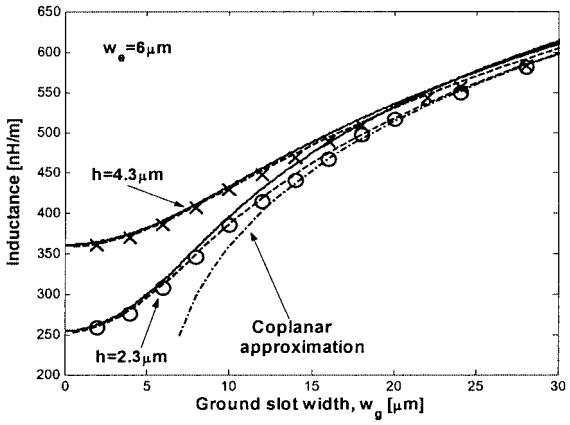

Fig. 9. HFSS simulated (circles and crosses) and calculated (solid lines) inductance. Also included is the result from an exact mapping (without the virtual conductor) using the MATLAB Schwarz–Christoffel toolbox ([Online]. Available: http://www.math.udel.edu/~driscoll/software/) according to [11]. The dashed–dotted line is a CPW approximation with the same ratio of w_e/w_g [7]. The HFSS simulated inductance is obtained from the simulated Z_0 and γ by replacing all SC and dielectric to air using (3) and (4).

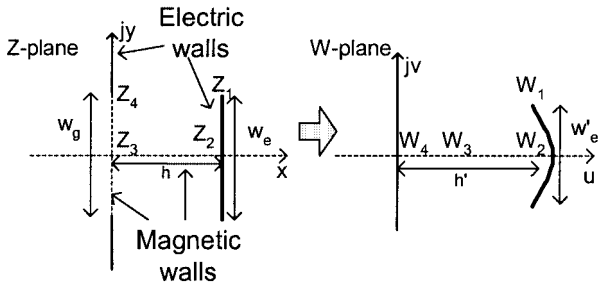

Fig. 10. Conformal mapping for evaluation of $C_{\rm even}$.

in Fig. 8. This approximation results in a very good agreement with HFSS simulations, as shown in Fig. 9. $C_{\rm odd}$ corresponds to the capacitance of a conventional microstrip [7]. $C_{\rm even}$ may be approximated by using the conformal mapping according to Fig. 10

$$W^2(Z) = \left(\frac{2Z}{w_g}\right)^2 + 1. \tag{24}$$

Specifically, the points W_1 and W_2 are expressed as

$$W_1^2 = W^2\left(h + j\frac{w_e}{2}\right) = \left(\frac{2h}{w_g} + j\frac{w_e}{w_g}\right)^2 + 1 \tag{25}$$

$$W_2^2 = W^2(h) = \left(\frac{2h}{w_g}\right)^2 + 1. \tag{26}$$

The shape of the strip in the W-plane is now distorted as indicated in Fig. 10. However, we have found that the capacitance is well approximated by assuming a microstrip with an average value for the strip height, i.e.,

$$\frac{w'_e}{h'} = \frac{4\,\mathrm{imag}(W_1)}{W_2 + \mathrm{real}(W_1)}. \tag{27}$$

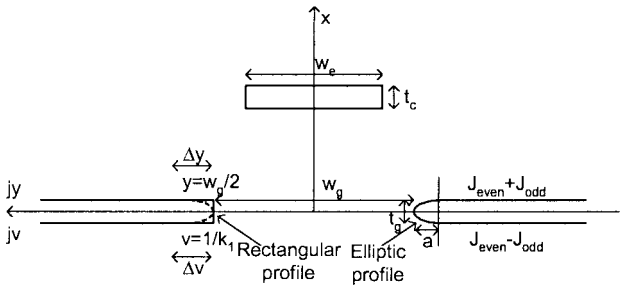

Fig. 11. Geometry for metal loss calculations. The y and v coordinates refer to Figs. 17 and 18 in the Appendix, respectively.

B. Ground-Plane Metal Conductor Losses

Using the virtual conductor formalism with the odd and even mode introduced in the above section, we may calculate the conductor loss elements R_C and R_{CG} in Fig. 2 with conformal-mapping techniques. In this section, we only present the result of the loss calculation obtained by the conformal mapping included in the Appendix.

As the odd and even modes are orthogonal (Fig. 11), we may treat each mode separately with a corresponding conductor resistance

$$R_{CG} = \frac{R_{\rm even} + R_{\rm odd}}{2}. \tag{28}$$

where $R_{\rm even}$ and $R_{\rm odd}$ are calculated by integrating the loss dissipation around the conductor surface [7]. Starting with the odd mode, the loss dissipation is given as (from (A17) in Appendix)

$$\frac{R_{\rm odd}}{R_m} = \frac{1}{2p_{o0}^2 C}\int_{1/k_1}^{\infty} \frac{dv}{(1+k_0^2v^2)\sqrt{(1+v^2)(1+k^2v^2)}} \tag{29}$$

where R_m is the skin-effect resistance

$$R_m = \frac{1}{\delta\sigma} = \sqrt{\frac{\omega\mu}{2\sigma}}. \tag{30}$$

The integral is evaluated numerically using the following solution for the Schwarz–Christoffel parameter problem:

$$\log(k) \approx -0.4357\frac{w_e}{h} + 2.6\cdot 10^{-3}\left(\frac{w_e}{h}\right)^2 \tag{31}$$

$$\log(k_e) \approx -0.4357\frac{w'_e}{h'} + 2.6\cdot 10^{-3}\left(\frac{w'_e}{h'}\right)^2 \tag{32}$$

where w'_e/h' is given by (27)

$$k_1 = k\sqrt{\frac{1-k_e^2}{k_e^2-k^2}} \tag{33}$$

$$k_0^2 = k^2\frac{K'(k)}{E'(k)} \tag{34}$$

$$C = \frac{2E'(k)h}{\pi} \tag{35}$$

$$p_{o0} = K'(k) \tag{36}$$

where K and E are the complete elliptic integrals of the first and second kind, respectively [7].

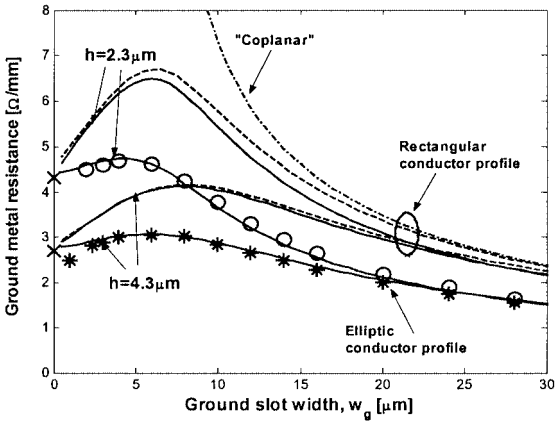

Fig. 12. HFSS simulated (stars and circles) and calculated ground metal resistance assuming an elliptic and rectangular conductor edge profile, respectively (solid lines). The dashed lines correspond to an exact mapping [11]. Also included is the corresponding loss for a CPW (dashed–dotted line) with corresponding w_e/w_g, and a microstrip (cross at $w_g = 0$) according to [7]. This figure illustrates data for $f_q = 80$ GHz, $w_e = 6$ μm, $t_g = 0.3$ μm, and $\sigma = 4.54 \cdot 10^5/\Omega \cdot$ cm.

For the even mode, the loss dissipation is given as

$$\frac{R_{\text{even}}}{R_m} = \frac{1}{2p_{e0}^2 C}\int_{1/k_1+\Delta v}^{\infty} \frac{\left(k^2+k_1^2\right)v^2 dv}{\left(1-k_1^2v^2\right)\left(1+k_0^2v^2\right)\sqrt{\left(1+v^2\right)\left(1+k^2v^2\right)}} \tag{37}$$

where

$$p_{e0} = K'(k_e). \tag{38}$$

Again, the integral has to be evaluated numerically. The lower integration limit is corrected by Δv in order to avoid the singularity that arises from the assumption of an infinitely thin conductor [7], [20]

$$\Delta v \approx \frac{dW}{dZ}\Delta y = \frac{\sqrt{\left(k_1^2+1\right)\left(k_1^2+k^2\right)}}{C\left(k_1^2+k_0^2\right)}\Delta y \tag{39}$$

where the value of Δy is determined from the assumed shape of the corners, and the thickness t_g of the ground conductor [20] (Fig. 11).

For a rectangular cross section

$$\Delta y \approx \frac{t_g}{290.8}. \tag{40a}$$

For an elliptic conductor cross section, where a is the main axis radius of the ellipse (Fig. 11)

$$\Delta y \approx \frac{t_g^2}{32a}. \tag{40b}$$

The calculated ground metal loss is compared to results from HFSS simulations in Fig. 12. The strip conductor is assumed here to be a perfect conductor. The conductor cross-sectional shape has been drawn as a rectangle in HFSS. However, the simulated loss corresponds to the calculation of an elliptical cross section.[2]

C. Strip Conductor Loss

The loss dissipation for the conductor strip is expressed as

$$R_C = \frac{R_m}{2p_{o0}^2 C}\int_1^{1/k}\left[\frac{p_{o0}u\sqrt{k^2+k_1^2}}{2p_{e0}\sqrt{1+k_1^2u^2}}+\frac{1}{2}\right]^2 \times \frac{du}{\left(1-k_0^2u^2\right)\sqrt{\left(1-u^2\right)\left(1-k^2u^2\right)}}. \tag{41}$$

The singularity at $u = 1/k_0$ has to be avoided [20] as outlined in the above section.

Note that, with typical strip parameters, according to Table I, the strip resistance is very close to the value of an isolated strip, given by the significantly simpler expression [7], [20]

$$R_C \approx \frac{R_m}{\pi^2 w_e}\ln\left(\frac{w_e}{\Delta y}\right). \tag{42}$$

Δy is given by (40) depending on the conductor thickness and assumed profile shape.

D. SC Loss

When we derived expressions for the quasi-TEM fields, we approximated the SC material as a perfect conductor for the electric field and an insulator for the magnetic field. This approximation can be justified in a low-frequency regime, as the induced longitudinal current in the substrate has a negligible effect on the transversal magnetic-field solution. This current will, however, lead to increased loss dissipation, modeled by R_{SC} in Fig. 2. Neglecting the transversal electrical field within the SC, the resulting current density is given as [21]

$$\nabla_T J_z = j\omega\sigma\nabla_T A_z. \tag{43}$$

Assuming that $E_z = 0$ on the ground metal, we may express J_z in the lower mesa part and along the slot opening as

$$J_z = j\omega\sigma A_z \tag{44}$$

where

$$A_z(x \geq 0, y) = A_{ze}(x, y) + A_{zo}(x, y). \tag{45}$$

A_{ze} and A_{zo} are the longitudinal components of the vector magnetic potential given by (A13) and (A14), and (x, y) refers to coordinates in the Z-plane, as defined in the Appendix. Inside the substrate $(x < 0)$, we may use the mode-matching method [18] in order to find a general expression for the potential by expanding the solution into Fourier series

$$A_z(x \leq 0, y) = \sum_{n=1}^{\infty} a_n \cos(\gamma_n y)e^{\gamma_n x} \tag{46}$$

where a_n is determined by assuming a continuous potential at the boundary $x = 0$. However, for a thin conducting SC layer

[2]We have found that HFSS (ver. 5.2) seems to effectively round off sharp conductor corners. The conductor loss obtained with conformal mapping for an ideal rectangular cross section is higher; this is also the case for a simulated microstrip loss compared to (42). Generally, using an elliptic conductor cross section with $a \approx 3t_c/4$ gives a good correspondence to HFSS simulations.

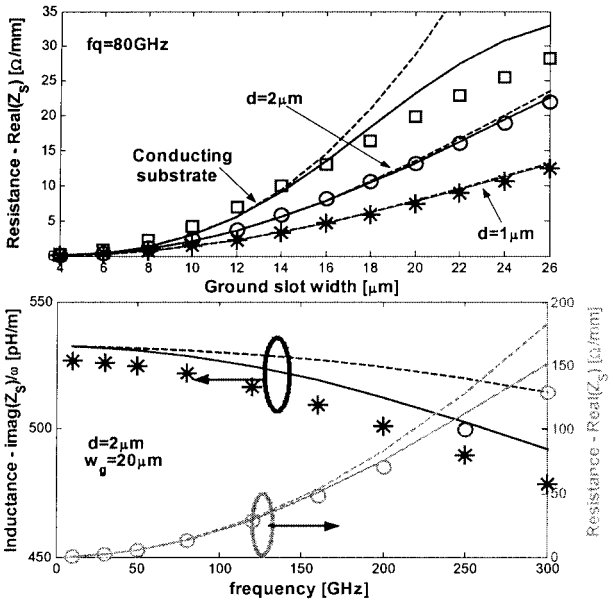

Fig. 13. Calculated and simulated Z_S as function of ground slot width (upper graph) and frequency (lower graph), respectively. This figure presents calculations according to the simple low-frequency model (dashed lines) where the resistance is proportional to ω^2, as well as the corrected HF model (solid lines). Geometrical parameters according to Table I with $h = 4.3$ μm and $\sigma = 370/\Omega \cdot$ cm. (Here, we have assumed a perfect conductivity of the metal.)

(small d in Fig. 1) with a *typical* shape for the potential, (46) is well approximated as

$$A_z\left(x \le 0, y\right) \approx A_{ze}\left(x = 0, y\right) e^{\pi x / w_g}. \tag{47}$$

This approximation may also be used to *indicate* the loss for a conductive substrate, as illustrated in Fig. 13. The loss dissipation in the substrate is then given as

$$\frac{2P_{LSC}}{\omega^2 I_L^2} \approx \frac{\sigma_{n-\text{sub}}\mu^2}{16 p_{e0}^2}\frac{w_g}{\pi}\left(1 - e^{-2\pi d/w_g}\right) \times C\int_{v=0}^{1/k1} \frac{o_e^2(v)\left(1 + k_0^2 v^2\right)}{\sqrt{\left(1+v^2\right)\left(1+k^2 v^2\right)}} dv \tag{48}$$

where $o_e(v)$ is given from (A9) and (A10). The remaining integral is evaluated numerically. The substrate conductor resistance is then obtained from (1) as follows:

$$R_{\text{SC}} = \frac{\omega^2 L^2}{P_{LSC}}\frac{|I_L|^2}{2}. \tag{49}$$

For a buried WG structure, we also need to include the loss dissipation in the lower part of the mesa as follows:

$$\frac{2P_{\text{LSCmesa}}}{\omega^2 I_L^2} \approx \frac{\sigma_{n\text{-mesa}}\mu^2}{16} \times w_a \int_{x=0}^{h_n} \left|\frac{o_{e1}}{p_{e0}} + \left(\frac{o_{e0} - o_{e1}}{p_{e0}} + \frac{o_{o0}}{p_{o0}}\right)\frac{x}{h}\right|^2 dx \tag{50}$$

where the mapped coordinates (o, p) are given by (A6)–(A8). The loss dissipation in the upper mesa section is normally neglected because of the low conductivity of p-doped InP. This addition is however simply treated in a similar manner, where E_z is now integrated from the upper conductor.

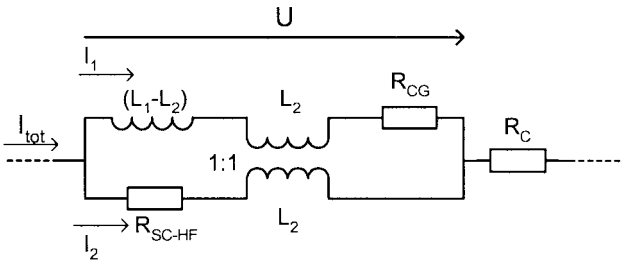

Fig. 14. Advanced equivalent circuit representing the impedance per unit length Z_s.

E. High-Frequency (HF) Limitation and Correction of the Basic Model

The model with a parallel resistor in Fig. 2 is sufficient for modulator design up to frequencies of typically 160 GHz or more. For higher frequencies or if a conductive substrate is used, the current induced in the SC [from (52) and (53)] may not be negligible and the inductance is reduced at higher frequencies. This represents a transition between a slow-wave mode and a skin-effect mode [19]. This situation can no longer be treated by the simple quasi-TEM model used thus far, in fact, the magnitude of the induced current from (52) can be used as an indication for the limit where a full-wave solution is required [22]. Nevertheless, by using the more advanced circuit model, illustrated in Fig. 14, the basic quasi-TEM model can be modified in order to include the effect of a nonnegligible current induced in the SC layers. As illustrated in Fig. 13, this correction extends the frequency limit in which the model is valid, however, we emphasize that when the magnitude of the substrate current is comparable to the ground metal current ($I_2 \approx I_1$ in Fig. 14), the result should only be seen as an approximation of the induced loss.

The current is divided here into two contributions representing the current in the metal ground I_1, as well as the current in the SC substrate I_2. The inductive coupling between the ground metal and substrate is represented with a mutual inductance L_2. The inductance for the current in the substrate (I_2) is here approximated to L_2 for simplicity. We then have (neglecting R_{CG})

$$\begin{pmatrix} U \\ U \end{pmatrix} = \begin{pmatrix} j\omega L_1 & j\omega L_2 \\ j\omega L_2 & R_{\text{SC-HF}} + j\omega L_2 \end{pmatrix}\begin{pmatrix} I_1 \\ I_2 \end{pmatrix}. \tag{51}$$

The current induced in the substrate is given by

$$\frac{I_2}{j\omega I_1} \approx \frac{\sigma\mu}{2p_{e0}}\frac{w_g}{\pi}\left(1 - e^{-\pi d/w_g}\right) \times C\int_{v=0}^{1/k1} \frac{o_e(v)\left(1 + k_0^2 v^2\right)}{\sqrt{\left(1+v^2\right)\left(1+k^2 v^2\right)}} dv. \tag{52}$$

For a BH structure, the additional current in the mesa section is given as

$$\frac{I_{2\text{-mesa}}}{j\omega I_1} \approx \frac{\sigma_{n\text{-mesa}}\mu}{4} \times w_a\left(\frac{o_{e1}}{p_{e0}}h_n + \left(\frac{o_{e0} - o_{e1}}{p_{e0}} + \frac{o_{o0}}{p_{o0}}\right)\frac{h_n^2}{2h}\right). \tag{53}$$

With this model, $R_{\mathrm{SC-HF}}$ is given by

$$R_{\mathrm{SC-HF}} = \frac{2P_{LSC}}{I_2^2} = \frac{2P_{LSC}}{\omega^2 I_1^2}\frac{|j\omega I_1|^2}{I_2^2} \tag{54}$$

where P_{LSC} is given by (48). Note that this is not the same value for R_{SC} that we used in the simple model.

Eliminating U in (51) gives

$$L_2 = L_1 - R_{\mathrm{SC-HF}}\frac{I_2}{j\omega I_1}. \tag{55}$$

Finally, the impedance per unit length Z_S according to the HF model is given as

$$Z_S = \frac{U}{I_1+I_2} = \frac{j\omega L_1 R_{\mathrm{SC-HF}} - \omega^2 L_2 (L_1 - L_2)}{R_{SC-HF} + j\omega (L_1 - L_2)}. \tag{56}$$

An example of calculated and simulated Z_S is plotted in Fig. 13.

V. Verification of a Simulated WG and Comparison With Experimental Work

A. Simulated WG Parameters

Thus far, we have only compared isolated parts of the model to the results of HFSS simulations. In this section, we verify that the calculated model also corresponds well to a simulation of a complete structure. Using the parameter values for a BH structure from Tables I and II, our model results in the following circuit parameters (basic model according to Fig. 2): $C_{\mathrm{int}} = 977$ pF/m, $C_{\mathrm{ext}} = 226$ pF/m, $R_p = 0.75\ \Omega$mm, $L = 372$ nH/m, $R_C = 786\ \Omega/(\mathrm{m}\sqrt{\mathrm{GHz}})$, $R_{CG} = 338\ \Omega/(\mathrm{m}\sqrt{\mathrm{GHz}})$, and $R_{\mathrm{SC}} = 15\ \mathrm{M}\Omega/\mathrm{m}$ (corresponding values for the advanced HF-model (Fig. 14) are: $L_2 = 212$ nH/m and $R_{\mathrm{SC-HF}} = 2.7\ \mathrm{M}\Omega/\mathrm{m}$). Here, we have assumed an elliptic conductor cross section in order to match the results from HFSS simulations (see Section IV-B). The resulting characteristic impedance and propagation factor are plotted in Fig. 15, and show a very good agreement with results obtained from full-wave simulations.

There is a small discrepancy at lower frequencies arising from the internal inductance $(L_i = R_c/\omega)$ [23] that is not included in our model. This effect is generally not important for the design of HF modulators, as the influence of the inductance is negligible at low frequencies.

B. Measured WG Parameters

We will here compare the model to measured data obtained from $l = 900$-μm–long test modulator structures according to Fig. 16. The WG is characterized using Picoprobe 67A ground–signal–ground (GSG) probes with 50-μm pitch and a standard on-wafer calibration reference. The test structures have a buried WG configuration with BCB cladding (for further details, see [4], [6], and [8]). The following WG geometry is estimated from scanning electron microscopy (SEM) picture data: $h \approx 3.7\ \mu$m, $h_n \approx 1.7\ \mu$m (n-InP $10^{18}/\mathrm{cm}^3$), $h_p \approx 1.6\ \mu$m (p-InP $5\cdot 10^{17}/\mathrm{cm}^3$), $h_a \approx 0.4\ \mu$m (i-InGaAsP/InP), $d \approx 0.3\ \mu$m (n-InGaAs $5\cdot 10^{18}/\mathrm{cm}^3$), $w_g \approx 6\ \mu$m, $t_c \approx 1.5\ \mu$m, $t_g \approx 0.3\ \mu$m. The structures have three different electrode widths (w_e) of 7, 13, and 25 μm and two different mesa widths (w_a) of approximately 1.9 and 2.9 μm.

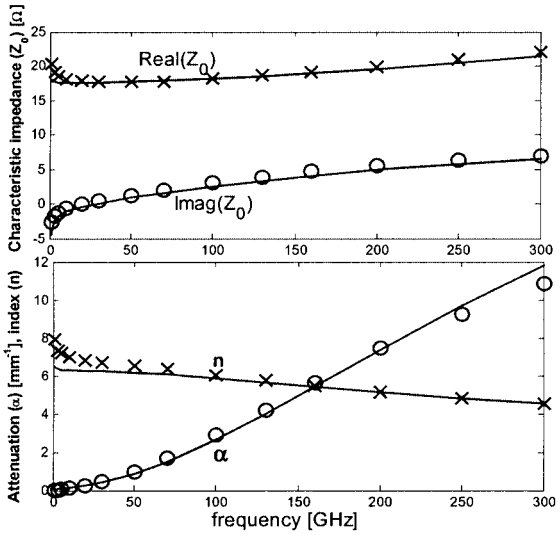

Fig. 15. Example of calculated (solid lines) TML parameters compared to simulated parameters. The geometry corresponds to a BH structure with parameters according to Tables I and II and $\varepsilon_r = 12.4$.

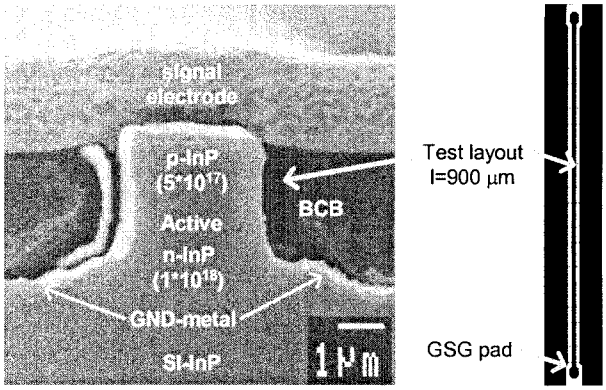

Fig. 16. Left-hand-side figure shows an SEM picture of the WG cross section, the right-hand-side figure shows the layout with pad configuration for a test structure with an electrode width of 13 μm. (The ground metal layout is not shown in the right-hand-side figure.)

The propagation factor γ is extracted from measured S-parameters from the trace (or eigenvalue sum) of the equivalent T-matrix [24]

$$2\cosh(\gamma l) = \frac{1}{S_{21}} + S_{12} - \frac{S_{11}S_{22}}{S_{21}}. \tag{57}$$

The characteristic impedance is extracted from the $ABCD$ [25] matrix as

$$Z_0 = 50\sqrt{\frac{(1+S_{11})(1+S_{22}) - S_{12}S_{21}}{(1-S_{11})(1-S_{22}) - S_{12}S_{21}}}. \tag{58}$$

In Figs. 17 and 18, we present the equivalent admittance and impedance per unit length obtained from (3) and (4).

We find the measured R_p in the Y_p network somewhat higher than expected. This resistance is normally dominated by the p-doped material. The nominal conductivity for p-InP with a doping of $5\cdot 10^{17}\ \mathrm{cm}^{-3}$ is $\sigma = 10/\Omega\cdot\mathrm{cm}$ [14], whereas the model curves plotted in Fig. 17 correspond to a conductivity of $\sigma = 4/\Omega\cdot\mathrm{cm}$. There can be several reasons for this discrepancy, for instance, passivation or uncertainty of the concentration of

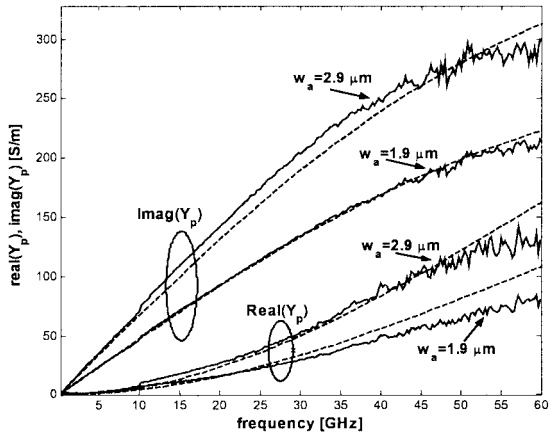

Fig. 17. Measured (solid) and calculated (dashed) admittance per unit length (Y_p) of test structures with an electrode width of 13 μm and mesa widths of 1.9 and 2.9 μm, respectively. The p-layer conductivity is here assumed to be $\sigma = 4/\Omega \cdot$ cm.

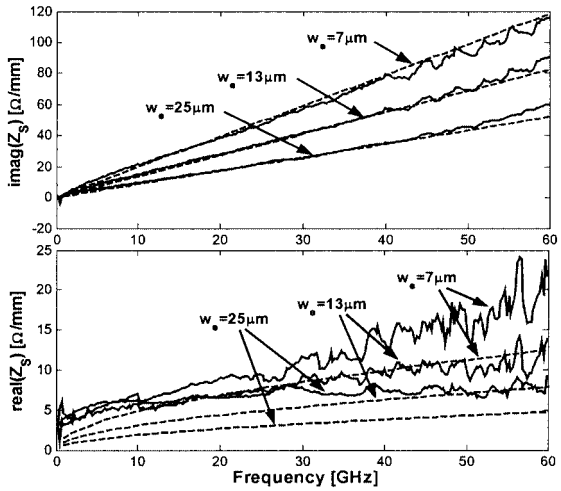

Fig. 18. Measured (solid) and calculated (dashed) impedance per unit length (Z_s) of test structures with a mesa width of 2.9 μm and electrode widths of 7, 13, and 25 μm, respectively.

acceptors. Nevertheless, the measurements and model show a correct tendency with varied mesa width.

Fig. 18 shows the measured and calculated impedance per unit length. As illustrated, there is a good correspondence for the imaginary part (inductance), while the real part is approximately 50% higher than calculated (here, we assume a rectangular conductor cross section). The model does not include effects related to surface or edge roughness of the conductor or the ground contact, respectively.

Due to the low p-conductivity of our test structures, the electrode resistance has a negligible contribution to the total attenuation.

VI. Conclusions

We have derived a calculation algorithm for the quasi-TEM TML circuit elements for a WG structure suitable as a TWEAM. The reactive circuit elements are derived in a closed-form expression, whereas the resistive elements require three (four for the HF model) numerical integrations. We emphasize that although this paper includes a lot of equations, the algebra is straightforward. The resulting circuit model is valid for a wide parameter range and a wide frequency range. The presented TML model shows very good agreement with the results obtained from HFSS simulations (given the assumptions related to conductor profiles discussed in Section IV-B).

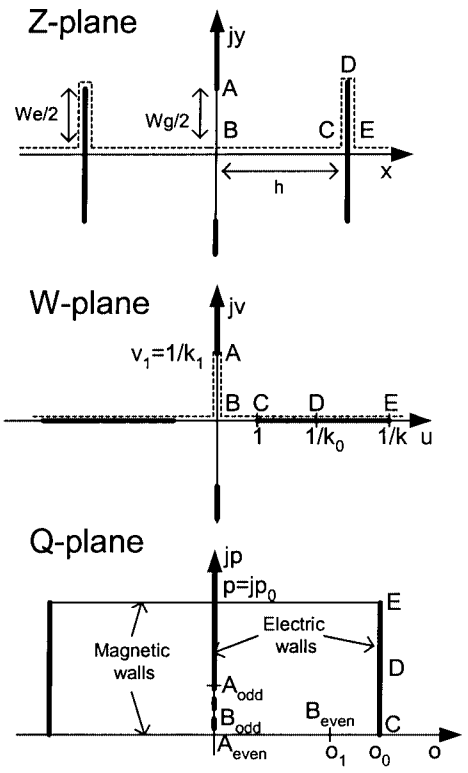

Fig. 19. Conformal mapping for evaluation of Z_s.

This correspondence is shown separately for each single element of the circuit model, as well as for the resulting characteristic impedance and propagation constant of the TML. In comparison with experimental data, we achieve a good agreement for the reactive circuit elements, and a correct tendency for the resistive circuit elements. We believe that the major part of the discrepancy can be traced from the difference between the idealized geometry (Fig. 1) and the processed structure (Fig. 16), together with the uncertainty about the correct material data (Table II).

Appendix
Conformal Mapping for Evaluation of Z_s

We use a standard microstrip Schwarz–Cristoffel transformation [7], which maps the strip conductor in the Z-plane to the real axis in the W-plane (Fig. 19)

$$\frac{dZ}{dW} = C\frac{1-k_0^2W^2}{\sqrt{(1-W^2)(1-k^2W^2)}}. \tag{A1}$$

An approximate solution to the parameter problem is given by (31)–(35). k_1 is obtained by solving the integral relation

$$\frac{w_g}{2} = C\int_{v=0}^{1/k_1}\frac{1+k_0^2v^2}{\sqrt{(1+v^2)(1+k^2v^2)}}dv \tag{A2}$$

which can be approximated according to (32).

For the even mode, the dashed line in the W-plane is mapped to the real axis in the T-plane as

$$T^2 = 1 + k_1^2 W^2. \tag{A3}$$

The real axis is then mapped to a rectangle in the Q-plane as follows:

$$\frac{dQ}{dW}_{\text{even}} = \frac{W\sqrt{k_1^2+k^2}}{\sqrt{(1-W^2)(1-k^2W^2)(1+k_1^2W^2)}}. \tag{A4}$$

For the odd mode, we map the real axis in the W-plane to a rectangle in the Q-plane as follows:

$$\frac{dQ}{dW}_{\text{odd}} = \frac{1}{\sqrt{(1-W^2)(1-k^2W^2)}}. \tag{A5}$$

The mapped points B, C and E are expressed as follows.

Odd mode:

$$o_{o0} = K(k) \text{ and } p_{o0} = K'(k). \tag{A6}$$

Even mode:

$$o_{e0} = K(k_e) \text{ and } p_{e0} = K'(k_e) \tag{A7}$$

where k_e is given by (33)

$$o_{e1} \approx o_{e0} - \frac{1}{\sqrt{1-k_e^2}} \cos^{-1}\left(\frac{1}{\sqrt{k_1^2+1}}\right). \tag{A8}$$

For the evaluation of the SC loss, the relation between the W- and Q-plane for the even mode along the slot opening in the ground plane (section AB) is given as

$$r = \sqrt{\frac{1-k_1^2v^2}{1+k_1^2}} = sn(o_e, k_e) \tag{A9}$$

where $sn(o,k)$ is the elliptic sine function with modulus k [7], o_e is well approximated as

$$\begin{aligned} o_e(v) =& sn^{-1}(r, k_e) \\ \approx& \max\left(\frac{1}{\sqrt{2(1+k_e^2)}} \ln\left|\frac{\sqrt{2}+r\sqrt{1+k_e^2}}{\sqrt{2}-r\sqrt{1+k_e^2}}\right|,\right. \\ & \left. K(k_e) - \frac{1}{\sqrt{1-k_e^2}}\cos^{-1}(r)\right). \end{aligned} \tag{A10}$$

Within the modulator mesa (section BC), the mapped coordinate is well approximated as

$$o_o(x, v=0) \approx \frac{x}{h} o_{o0}, \qquad x \le h \tag{A11}$$

$$o_e(x, v=0) \approx o_{e1} + (o_{e0} - o_{e1})\frac{x}{h}, \qquad x \le h \tag{A12}$$

for the odd and even modes, respectively.

The magnetic potential $\mathbf{A}$ in the Q-plane is for the even and odd modes, respectively,

$$A_{ze}(o_e, p_e) = \frac{I_e \mu_0}{2p_{e0}} o_e \tag{A13}$$

$$A_{zo}(o_o, p_o) = \frac{I_o \mu_0}{2p_{o0}} o_o \tag{A14}$$

where $I_e = I_o = I_{\text{tot}}/2$ is the current for the even and odd modes, respectively.

The transversal components of the magnetic field (H_T) for each mode in the Q-plane is then given according to the quasi-TEM approximation

$$\bar{H}_{TQ} = -\frac{1}{\mu_0}\hat{z} \times (\nabla_Q A_z) = -\frac{I}{2p_0}\hat{p}. \tag{A15}$$

The sheet current density is then given in the Z-plane as (for each mode, respectively)

$$J_{Zn} = \bar{H}_{TZ} = \bar{H}_{TQ}\frac{dQ}{dZ} = \frac{I_n}{2p_{n0}}\frac{dQ}{dZ}. \tag{A16}$$

The power loss dissipation is then obtained by integrating along the imaginary axis in the W-plane as follows:

$$\frac{2P_{Ln}}{R_m I_n^2} = \frac{2}{4p_{n0}^2}\int_{v=1/k_1}^{\infty}\left|\frac{dQ}{dW}\right|^2\left|\frac{dW}{dZ}\right| dv. \tag{A17}$$

ACKNOWLEDGMENT

The authors would like to thank Dr. E. Berglind, Royal Institute of Technology, Stockholm, Sweden, for useful discussions.

REFERENCES

[1] Y. Akage, K. Kawano, S. Oku, R. Iga, H. Okamoto, Y. Miyamoto, and H. Takeuchi, "Wide bandwidth of over 50 GHz traveling wave electrode electroabsorption modulator integrated DFB lasers," *Electron. Lett.*, vol. 37, no. 5, pp. 299–300, 2001.

[2] Y.-J. Chiu, H.-F. Chou, V. Kaman, P. Abraham, and J. E. Bowers, "High extinction ratio and saturation power traveling-wave electroabsorption modulator," *IEEE Photon. Technol. Lett.*, vol. 14, pp. 792–794, June 2002.

[3] G. L. Li, S. A. Pappert, P. Mages, C. K. Sun, W. S. C. Chang, and P. K. L. Yu, "High-saturation high-speed traveling-wave InGaAsP–InP electroabsorption modulator," *IEEE Photon. Technol. Lett.*, vol. 13, pp. 1076–1078, Oct. 2001.

[4] S. Irmscher, R. Lewén, and U. Eriksson, "InP/InGaAsP high-speed traveling-wave electro-absorption modulators with integrated termination resistors," *Photon. Technol. Lett.*, vol. 14, pp. 923–925, July 2002.

[5] G. L. Li, S. K. Sun, S. A. Pappert, W. X. Chen, and P. K. L. Yu, "Ultrahigh-speed traveling-wave electroabsorption modulator—Design and analysis," *IEEE Trans. Microwave Theory Tech.*, vol. 47, pp. 1177–1183, July 1999.

[6] S. Irmscher, R. Lewén, and U. Eriksson, "Influence of electrode width on high-speed performance of traveling-wave electro-absorption modulators," presented at the 13th Int. Indium Phosphide and Related Materials Conf., Nara, Japan, May 2001, Paper WA3-3.

[7] R. E. Collin, *Foundation for Microwave Engineering*, 2nd ed, Singapore: McGraw-Hill, 1992.

[8] S. Irmscher, R. Lewén, and U. Eriksson, "Microwave properties of ultra-high-speed traveling-wave electro-absorption modulators for 1.55 μm," presented at the Integrated Photonics Research Conf., Monterey, CA, June 2001, Paper IME2-1.

[9] H. H. Liao, K. K. Loi, C. W. Tu, P. M. Asbeck, and W. S. C. Chang, "Microwave structures for traveling-wave MQW electro-absorption modulators for wide band 1.3 mm photonic links," *Proc. SPIE*, vol. 3006, pp. 291–300, 1997.

[10] K. Giboney, M. Rodwell, and J. Bowers, "Traveling-wave photodetector theory," *IEEE Trans. Microwave Theory Tech.*, vol. 45, pp. 1310–1319, Aug. 1997.

[11] M. Goano, F. Bertazzi, P. Caravelli, G. Ghione, and T. A. Driscoll, "A general conformal-mapping approach to the optimum electrode design of coplanar waveguides with arbitrary cross section," *IEEE Trans. Microwave Theory Tech.*, vol. 49, pp. 1573–1580, Sept. 2001.

[12] S. Zhang, "Traveling-wave electroabsorbtion modulators," Ph.D. dissertation, Dept. Elect. Comput. Eng., Univ. California at Santa Barbara, Santa Barbara, CA, 1999.

[13] M. Shirai, H. Arimoto, K. Watanbe, A. Taike, K. Shinoda, J. Shimizu, H. Sato, T. Ido, T. Tsuchiya, M. Aoki, and T. Tsuji, "Impedance-controlled-electrode (ICE) semiconductor modulators for 1.3-μm 40 Gbit/s tranceivers," in *Proc. Eur. Opt. Commun. Conf.*, vol. 4, 2002, Paper 9.5.4.

[14] *Properties of Indium Phosphide*, ser. EMIS datareviews 6. London, U.K.: INSPEC, 1991.
[15] Y. R. Kwon, V. M. Hietala, and K. S. Champlin, "Quasi-TEM analysis of 'slow-wave' mode propagation on coplanar microstructure MIS transmission lines," *IEEE Trans. Microwave Theory Tech.*, vol. MTT-35, pp. 545–551, June 1987.
[16] H. A. Wheeler, "Transmission-line properties of parallel strips separated by a dielectric sheet," *IEEE Trans. Microwave Theory Tech.*, vol. MTT-13, pp. 172–186, Mar. 1965.
[17] G. Ghione and C. U. Naldi, "Coplanar waveguides for MMIC applications: Effect of upper shielding, conductor backing, finite-extent ground planes, and line-to-line coupling," *IEEE Trans. Microwave Theory Tech.*, vol. MTT-35, pp. 160–267, Mar. 1987.
[18] Y. Fukuoka, Y.-C. Shih, and T. Itoh, "Analysis of slow-wave coplanar waveguide for monolithic integrated circuits," *IEEE Trans. Microwave Theory Tech.*, vol. MTT-31, pp. 567–573, July 1983.
[19] H. Hasegawa, M. Furukawa, and H. Yanai, "Properties of microstrip line on Si–SiO_2 system," *IEEE Trans. Microwave Theory Tech.*, vol. MTT-19, pp. 869–881, Nov. 1971.
[20] L. Lewin, "A method of avoiding edge current divergence in purturbation loss calculations," *IEEE Trans. Microwave Theory Tech.*, vol. MTT-32, pp. 717–719, 1984.
[21] M. J. Tsuk and J. A. Kong, "A hybrid method for the calculation of the resistance and inductance of transmission lines with arbitrary cross sections," *IEEE Trans. Microwave Theory Tech.*, vol. 39, pp. 1338–1347, Aug. 1991.
[22] F. Mesa, G. Cano, F. Medina, R. Marques, and M. Horno, "On the quasi-TEM and full wave approaches applied to coplanar multistrip on lossy dielectric layered media," *IEEE Trans. Microwave Theory Tech.*, vol. 40, pp. 524–531, Mar. 1992.
[23] H. A. Wheeler, "Formulas for the skin effect," *Proc. IRE*, vol. 30, pp. 412–424, Sept. 1942.
[24] H.-J. Eul and B. Shiek, "A generalized theory and new calibration procedures for network analyzer self-calibration," *IEEE Trans. Microwave Theory Tech.*, vol. 39, pp. 724–731, Apr. 1991.
[25] D. M. Pozar, *Microwave Engineering*. Reading, MA: Addison-Wesley, 1990, pp. 231–235.

Robert Lewén was born in Stockholm, Sweden, in 1971. He received the M.Sc. degree in electrical engineering from the Royal Institute of Technology (KTH), Stockholm, Sweden, in 1997, and is currently working toward the Ph.D. degree in electrical engineering at KTH.

Since 2001, he has also been with Optillion AB, Stockholm, Sweden. His research interests include HF electrical interfaces for EAMs and p-i-n photodiodes.

Stefan Irmscher received the M.S. degree in electrical engineering from the Technical University Berlin, Berlin, Germany, in 1998, and is currently working toward the Ph.D. degree at the Royal Institute of Technology, Stockholm, Sweden.

He is involved with the design, fabrication, and characterization of high-speed modulators for optical telecommunications.

Urban Eriksson was born in Stockholm, Sweden, in 1967. He received the M.S. degree in applied physics and Ph.D. degree in electrical engineering from the Royal Institute of Technology, Stockholm, Sweden, in 1994 and 1999, respectively. His dissertation concerned fabrication issues of InP opto-electronic integrated circuits involving various types of devices such as HBTs, edge-emitting lasers, long-wavelength vertical-cavity surface-emitting lasers (VCSELs), and photodiodes.

From 1997 to 1998, he was with the NTT System Electronics Laboratories, where he was involved with the integration of HBTs with the unitraveling carrier photodiode. In 2000, he joined Optillion AB, Stockholm, Sweden, where he is involved with the development of HF opto-electronic devices.